ADVANCED FUNCTIONAL MATERIALS
www.afm-journal.de

A Waterproof Ion-Conducting Fluorinated Elastomer with 6000% Stretchability, Superior Ionic Conductivity, and Harsh Environment Tolerance

Peiru Shi, Yufeng Wang, Kening Wan, Chao Zhang, and Tianxi Liu*

The development of ionic conductors with extreme stretchability, superior ionic conductivity, and harsh-environment resistance is urgent while challenging because the tailoring of these performances is mutually exclusive. Herein, a hydrophobicity-constrained association strategy is presented for fabricating a liquid-free ion-conducting fluorinated elastomer (ICFE) with microphase-separated structures. Hydrophilic nanodomains with long-range ordering and selectively enriched Li ions provided high-efficient conductive pathways, yielding impressive room-temperature ionic conductivity of 3.5×10^{-3} S m^{-1}. Hydrophobic nanodomains with abundant and reversible hydrogen bonds endow the ICFE with superior damage-tolerant performances including ultrastretchability (>6000%), large toughness (17.1 MJ m^{-3}) with notch insensitivity, antifatigue ability, and high-efficiency self-healability. Due to its liquid-free characteristic and surface-enriched hydrophobic nanodomains, the ICFE demonstrates an extreme temperature tolerance (−20 to 300 °C) and unique underwater resistance. The resultant ICFE is assembled into a proof-of-concept skin-inspired sensor, showing impressive capacitive sensing performance with high sensitivity and wide-strain-range linearity (gauge factor to 1.0 in a strain range of 0–350%), excellent durability (>1000 cycles), and unique waterproofness in monitoring of complex human motions. It is believed that the hydrophobicity-constrained association method boosts the fabrication of stretchable ionic conductors holding a great promise in skin-inspired ionotronics with harsh-environment tolerance.

1. Introduction

Stretchable electronics [1] with high mechanical flexibility and nonplanar compliance have shown broad prospects in the emerging fields of health monitoring,[2] soft robotics[3] and human-machine interfaces.[4] Stretchable conductors, as the core component of stretchable electronics, are the key material basis for realizing the rapid development of stretchable electronics.[5] Ionic conductors by using mobile ions as the charge carrier are expected to possess unique features including high intrinsic stretchability, transparency and biocompatibility, which are overwhelmingly difficult or even impossible to be achieved by conventional electronic conductors.[6] However, the stretchable ionic conductors are usually faced with complex and extreme environments in the practical applications of undergoing large deformations, wide-range temperatures and high-humidity environments. Additionally, when stretchable ionic conductors are subjected to continuous mechanical loadings from dynamic environments, inevitable microcracks and mechanical damages cannot be suppressed. Therefore, the development of stretchable ionic conductors with high mechanical robustness and outstanding tolerance to harsh environments is of great significance for the next-generation stretchable electronics yet challenging.

Ionogels,[7] which are derived from a 3D polymer network with space confined ionic liquids (ILs), are an ideal candidate for stretchable ionic conductors because of their high ionic conductivity and excellent thermal/chemical stability. They have been developed to solve bottleneck problems of hydrogels under harsh environments including dehydration at high temperature and freezing at subzero temperature. However, ionogels containing large amounts of ILs are likely to absorb moisture in high humidity, and ILs tend to leak when being subjected to mechanical forces (e.g., squeezing).[8] Although the encapsulation of ILs with elastomer layers is an efficient strategy to improve their long-term stability, it is immensely restricted by the complicated manufacturing process and the weak interfacial interaction between the elastomer layers and ionogels. More recently, the emerging liquid-free ion-conducting elastomers

P. Shi, Y. Wang, C. Zhang, T. X. Liu
State Key Laboratory for Modification of Chemical Fibers and Polymer Materials
College of Materials Science and Engineering
Donghua University
Shanghai 201620, P. R. China
E-mail: czhang@dhu.edu.cn

K. Wan
School of Engineering and Materials Science
Queen Mary University of London
Mile End Road, London E1 4NS, UK

T. X. Liu
Key Laboratory of Synthetic and Biological Colloids
Ministry of Education
School of Chemical and Material Engineering
Jiangnan University
Wuxi 214122, P. R. China

The ORCID identification number(s) for the author(s) of this article can be found under https://doi.org/10.1002/adfm.202112293.

DOI: 10.1002/adfm.202112293

like solid-state electrolytes are capable of realizing ion migration through a repetitive complexation/decomplexation process of alkali ions in the amorphous regions of polyether.[9] Nevertheless, these liquid-free ion-conducting elastomers generally exhibit an unsatisfactory stretchability, toughness, self-healability and moisture/heat-resistant performance, which cannot meet the great demands of next-generation stretchable electronics with high durability. Therefore, the development of liquid-free ion-conducting elastomers with harsh-environment tolerances by combining features of notch insensitivity, autonomous healability and moisture/temperature resistance is crucial yet still a huge challenge.

Herein, we present a hydrophobicity-constrained association strategy for fabricating an ion-conducting fluorinated elastomer (ICFE) with a microphase-separated structure. The ICFE consists of lithium bis(trifluoromethane sulfonimide) (LiTFSI) salts and a random copolymer network of poly(2,2,3,4,4,4-hexafluorobutyl acrylate)-random-poly(oligoethylene glycol methyl ether acrylate) (PHFBA-r-OEGA). The lithium cations (Li^+) and organic fluorinated anions ($TFSI^-$) of LiTFSI are selectively enriched in the hydrophilic and hydrophobic microphases of the ICFE, respectively. Li^+ ions are enriched in the hydrophilic OEGA microphase due to the strong coordination between the Li^+ ions and oxygen atoms, thus forming a 3D ion transport channel among the ICFE. The $TFSI^-$ ions are concentrated in the hydrophobic fluorinated microphase due to the "fluorous effect" between the $TFSI^-$ and fluorinated segments, thus forming a physically cross-linked network with high dynamic reversibility. The hierarchically responsive microphase-separated structure enables the resultant ICFE with extreme stretchability (>6000%), high mechanical strength (770 kPa), high toughness (171 MJ m^{-3}), tearing resistance with fracture energy up to 22.3 kJ m^{-2}, and superior high ionic conductivity to 3.5×10^{-3} S m^{-1} at 25 °C. Moreover, the ICFE demonstrates superhigh elasticity and self-recoverability, allowing its dimensional recovery even after being stretched up to 40 times its original length. Due to its liquid-free and waterproof features, the as-obtained ICFE demonstrates the unique combinations of wide-temperature resistance (−20 to 300 °C), high moisture and underwater resistance (long-term stability in 99% relative humidity) and high-efficiency self-healability (healing efficiency to 100% for 12 h at room temperature). As a proof-of-concept, a skin-inspired ionic sensor using the ICFE as a stretchable conductor is assembled, demonstrating excellent capacitive strain-sensing performances with high sensitivity, linear gauge factor up to 1 over a wide strain range of 0–350%, long-term cycle stability with uninterrupted properties after 1000 cycles, fast response time within 0.3 s, and unique waterproofness in real-time and rapid monitoring physiological motions. This work therefore provides a new path of hydrophobicity-constrained association strategy for developing liquid-free ion-conducting elastomers with high mechanical robustness, high ionic conductivity, outstanding tolerances to harsh environments.

2. Results and Discussion

The ICFE was synthesized via hydrophobicity-constrained association. Photoinitiated free-radical copolymerization of 2,2,3,4,4,4-hexafluorobutyl acrylate (HFBA) and oligoethylene glycol methyl ether acrylate (OEGA) in bulk was initiated by a photoinitiator of 2,2-diethoxyacetophenone (DEAP). LiTFSI, an organic lithium salt widely used in solid polymer electrolytes, was employed as a salt additive to achieve ionic conductivity. Thus, the as-formed ICFE is liquid-free and has a bi-continuous microphase-separated structure containing both the hydrophobic and hydrophilic nanodomains, which is illustrated in **Figure 1**a. The concentration of LiTFSI within the PHFBA-r-OEGA was tailored from 0.5, 1, 1.5 to 2 M, and the corresponding ICFE samples are named as the ICFE-0.5M, ICFE-1M, ICFE-1.5M, and ICFE-2M, respectively. Different HFBA/OEGA molar ratios (5/1, 10/1, and 20/1) were also intensely investigated because they influence the microphase-separated structure of the ICFE. Gel permeation chromatography (GPC) was performed to measure the molecular weight and molecular weight distribution of the ICFE-1.5M with the HFBA/OEGA molar ratio of 10/1. The number-average molecular weight (M_n) of the ICFE-1.5M is calculated as $\approx 8.0 \times 10^4$ g mol^{-1} with a relatively low polydispersity index (PDI) of 1.51 (Figure S1, Supporting Information).

Transmission electron microscopy (TEM) and atom force microscopy (AFM) characterizations were performed to investigate the as-formed microphase-separated structure among the ICFE. TEM images of the ICFE-1.5M indicate the formation of the bi-continuous microphase-separated structure, where the dark and light-colored regions refer to the hydrophilic and hydrophobic nanodomains (Figure 1b,c), respectively. It is observed that the hydrophilic nanodomain is continuously distributed within the hydrophobic nanodomain, which is also supported by the AFM phase image (Figure 1d). Small-angle X-ray scattering (SAXS) measurements were performed to further confirm the microphase-separated structure of the ICFE-1.5M (Figure S2, Supporting Information). The peak appears at a scattering vector magnitude (q) value of 0.2 nm^{-1}, indicating long-range ordering of the hydrophilic nanodomain within the ICFE-1.5M.[10] The periodicity representing the average distance between the hydrophilic nanodomains is calculated as 31.4 nm for the ICFE-1.5M. Organic salt-type LiTFSI is critical for the stability of the bi-continuous microphase-separated structure of the ICFE. The Li^+ ions are preferentially coordinated with the ether oxygen atoms from the OEGA,[11] which are capable of transporting through intrachain or interchain hoppings in the hydrophilic nanodomain through the breakage and reconstruction of coordinating bonds.[12] Meanwhile, $TFSI^-$ ions tend to concentrate in the hydrophobic nanodomain owing to the "fluorous effect" between the $TFSI^-$ and the fluorinated segment from the HFBA.[13] Scanning transmission electron microscopy (STEM) observation and corresponding EDS elemental mappings further demonstrate the selective distribution of $TFSI^-$ ions within the observation area of ultrathin-section ICFE-1.5M sample (Figure S3, Supporting Information). It could be observed that there were almost no fluorine (F) elements surrounding the oxygen (O) elements, whereas the characteristic sulfur (S) elements within the $TFSI^-$ ions were accompanied by F elements within the fluorinated microphases. The selective distribution of cations (Li^+) and anions ($TFSI^-$) plays a key role in stabilizing the bi-continuous microphase-separated structure with balanced charges.

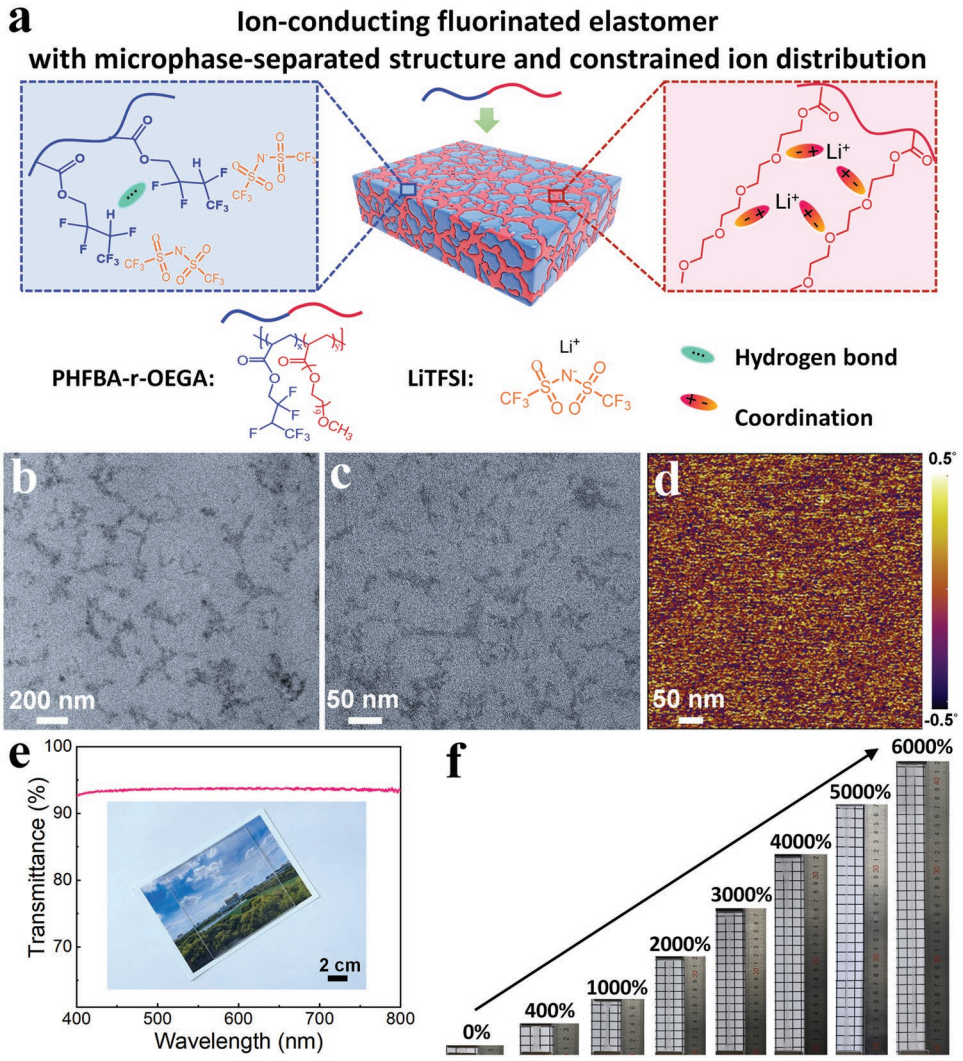

Figure 1. Design principle of the ICFE. a) Schematic illustration of the ICFE with a microphase-separated structure. b,c) TEM images and d) AFM phase image of the ICFE. e) UV–vis spectra of a 0.2 mm thickness ICFE film. Inset showing a photograph of the ICFE on a quartz plate. f) Photographs showing the ICFE being stretched at a strain from 0 to 6000%.

Figure 1e shows that the as-obtained ICFE exhibits high transparency owing to the phase separation only taking place at the nanoscale. The 0.2 mm-thickness ICFE-1.5M has an average transmittance of 93.6% in the visible light wavelength range of 400–800 nm. After successfully dissolving LiTFSI in the monomer solution, another kind of lithium salt, lithium nitrate ($LiNO_3$), fails to obtain a transparent precursor solution of monomers (Figure S4, Supporting Information), which is due to the absence of physical interactions between the NO_3^- and fluorinated segments leading to the insolubility of $LiNO_3$. Besides, the ICFE-1.5M also possesses an ultrahigh stretchability up to a uniaxial strain of 6000% (Figure 1f, Movie S1, Supporting Information, speed of 20 times the real time), and to our best knowledge, it is a remarkable value among the stretchable liquid-free ion-conducting elastomers so far.[14]

The interactions between PHFBA-r-OEGA and LiTFSI were investigated by attenuated total reflection flourier transform infrared spectroscopy (ATR-FTIR). From **Figure 2**a,b, the absorption peaks of PHFBA-r-OEGA at 1751 and 1150 cm^{-1} are assigned to the stretching vibrations of C=O and C−O−C, respectively. With the LiTFSI concentration increasing from 0 to 2 M, the absorption peak of the C=O gradually broadens and the corresponding intensities decline, and the absorption peak of the C−O−C shifts to relatively low wavenumbers from 1150 to 1134 cm^{-1}. These changes clearly indicate the presence of the coordination between Li^+ ions and O atoms.[15] Meanwhile, two SO_2 antisymmetric stretching vibration peaks at 1349 and 1329 cm^{-1}, as well as an SNS antisymmetric stretching vibration peak at 1057 cm^{-1} all shift to relatively high wavenumbers (Figure S5 and Table S1, Supporting Information), suggesting an increased electron cloud density around the SO_2 and SNS groups from the $TFSI^-$.[7a,16] This is because Li^+ ions are pulled away by the coordinated O atoms in the OEGA, resulting in a weak Coulombic force between Li^+ and $TFSI^-$. It is noteworthy that there is no coordination between the fluorine (F) atoms and Li^+ ions due to the inability of F atoms to act as Lewis donors.[17] In addition, the C-H bending originating from HFBA shifts from 1452 to 1455 cm^{-1}, implying the formation

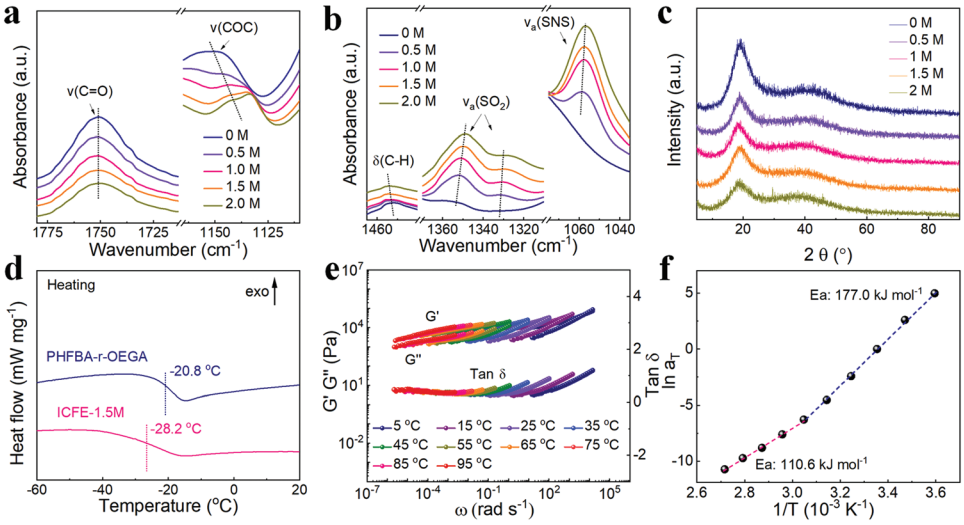

Figure 2. Structural and compositional characterizations. a,b) ATR-FTIR spectra and c) XRD patterns of ICFE with various LiTFSI concentrations. d) DSC thermograms of PHFBA-r-OEGA and ICFE-1.5M from –60 to 20 °C. e) Frequency dependence of the storage modulus G', loss modulus G'', and loss factor tan δ of ICFE-1.5M. f) Temperature dependence of shift factors of ICFE-1.5M from Arrhenius equations of (e).

of hydrogen bonds between H atoms and F atoms within the fluorinated segments.[18]

X-ray diffraction (XRD) analysis of PHFBA-r-OEGA and ICFE was conducted to study the crystalline structure of the ICFE. The PHFBA-r-OEGA displays diffraction patterns of the ordering of ether segments at $2\theta = \approx 20°$ (Figure S6, Supporting Information) and the corresponding intensity is weakened and broadened with the addition of LiTFSI, indicating a decreased crystallinity of ICFE (Figure 2c).[19] It is because the LiTFSI plasticizes the polymer matrix, which is further proved by the differential scanning calorimetry (DSC) results. The glass transition temperature (T_g) of PHFBA-r-OEGA decreased from –20.8 to –28.2 °C upon the addition of 1.5 M LiTFSI (Figure 2d). The plasticizing effects of LiTFSI on PHFBA and POEGA are also observed from DSC curves (Figure S7, Supporting Information).

Dynamically viscoelastic behaviors of ICFE were recorded by frequency sweep measurements at different temperatures. Figure 2e shows the master curves of the storage moduli (G'), loss moduli (G''), and loss factor (tan δ) of the ICFE-1.5M at a reference of 25 °C using the time-temperature superposition principle.[20] Notably, the G' values are greater than the G'' values over the entire angular frequency range from 10^{-6} to 10^{4} rad s^{-1}, indicating that the ICFE-1.5M exhibits a solid-like elasticity behavior.[21] The apparent activation energy (E_a) of ICFE-1.5M calculated by the Arrhenius equation (Equation S1, Supporting Information) varies over a wide range of 110.6–177.0 kJ mol^{-1}, suggesting a wide distribution of the bi-continuous phase structure with different strengths (Figure 2f). In addition, the E_a of ICFE-1.5M is higher than that of the supramolecular networks cross-linked by multiple dynamic bonds (41–96 kJ mol^{-1}).[22] This explains the formation of high-strength and toughness ICFE without covalent crosslinking.

The ionic conductivity of ICFE can be tuned by tailoring the LiTFSI concentration and the OEGA content within the ICFE (**Figure 3**a, Table S2, Supporting Information). Three kinds of ICFE with HFBA/OEGA molar ratios of 5/1, 10/1, and 20/1 upon the addition of 0.5 M LiTFSI exhibit high room-temperature ionic conductivities of 0.9×10^{-3}, 0.3×10^{-3}, and 0.2×10^{-3} S m^{-1}, respectively. When the LiTFSI concentration increases from 0.5 to 2 M, the ionic conductivities of these ICFE reach up to 11.4×10^{-3}, 8.1×10^{-3}, and 5.6×10^{-3} S m^{-1}, respectively. This is ascribed to the increase of the effective number of mobile ions in ICFE. Besides, the ionic conductivity of ICFE increases slightly with the HFBA/OEGA molar ratio tailoring from 20/1 to 5/1 at the same LiTFSI concentration, revealing that the hydrophilic nanodomain assembled by OEGA serves as an effective lithium-ion transport channel and provides a high ionic conductivity for the ICFE.[14b,23] In addition, the presence of hydrophobic nanodomains also motivates the Li^+ ions to transport because highly electronegative F atom reduces the nucleophilicity of the O atoms in the ether group, resulting in a relatively low binding strength between the Li^+ ion and O atom.[24]

The ICFE also exhibits relatively high ion conductivities under high temperatures (Figure 3b, Table S3, Supporting Information). For example, the ICFE-1.5M samples with HFBA/OEGA molar ratios of 5/1, 10/1, and 20/1 have the ion conductivities of 6.4×10^{-3}, 3.5×10^{-3}, and 2.8×10^{-3} S m^{-1} at 25 °C, respectively. When the temperature reaches 200 °C, the ionic conductivities of these ICFE samples significantly increase to 13.6×10^{-2}, 9.8×10^{-2}, and 7.7×10^{-2} S m^{-1}, respectively. The temperature-dependent conductivity behaviors of the ICFE obey the Vogel–Tammann–Fulcher (VTF) equation that is used to describe the ion transport behavior within a polymer electrolyte.[25] In addition, the OEGA content-dependent conductivity behaviors of ICFE are also observed in Figure 3b. Furthermore, the ionic conductivities of POEGA-1.5M, PHBFA-1.5M, and ICFE-1.5M with the HFBA/OEGA molar ratio of 10/1 at 25 °C are shown in Figure 3c. The ionic conductivity of POEGA-1.5M is 2.0×10^{-2} S m^{-1}, which is nearly two orders of magnitude higher than 2.7×10^{-4} S m^{-1} of PHFBA-1.5M, further confirming that the hydrophilic nanodomain plays the key role in

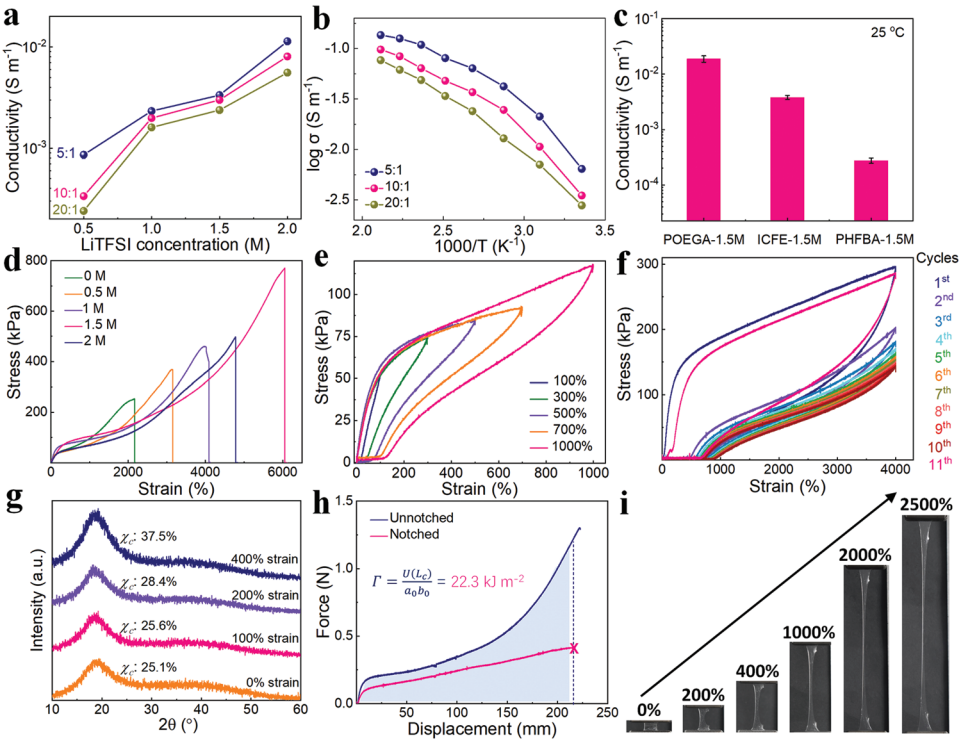

Figure 3. Ionic conductivity and mechanical performance. a) Ionic conductivities of PHFBA-r-OEGA as a function of various LiTFSI concentrations with HFBA/OEGA molar ratios of 5/1, 10/1, and 20/1, respectively. b) Temperature dependence of ionic conductivities of ICFE-1.5M with various HFBA/OEGA molar ratios. c) Ionic conductivities of POEGA-1.5M, ICFE-1.5M, and PHFBA-1.5M. d) Tensile stress–strain curves of ICFE with various LiTFSI concentrations. e) Cyclic stress–strain curves of ICFE-1.5M under various strains. f) Hysteresis loading-unloading tests of ICFE-1.5M upon being stretched to 4000% strain with the resting time of 2 h. g) XRD patterns of ICFE-1.5M under various strains. h) Force versus displacement for unnotched and notched ICFE-1.5M for fracture energy. i) Digital photographs of notched ICFE-1.5M being stretched from 0 to 2500%.

improving ionic conductivity. As expected, the ICFE-1.5M has an ionic conductivity of 3.5×10^{-3} S m^{-1}, which is between that of POEGA-1.5M and PHFBA-1.5M.

Ionic conductivity of the ICFE-1.5M exhibits long-term stability in an open-air environment for over 100 h (Figure S8, Supporting Information). The ICFE-1.5M could still maintain a stable ionic conductivity after being immersed in water for 72 h (Figure S9, Supporting Information). In striking contrast to the liquid-free ion-conducting elastomers in literature (Table S4, Supporting Information),[14b-d,26] the ICFE could achieve relatively high ionic conductivities with the same LiTFSI concentration. Intriguingly, it is easy to further enhance the ionic conductivity of the ICFE by increasing the OEGA contents.

Figure S10a (Supporting Information) shows the tensile stress–strain curves of PHFBA, POEGA and three PHFBA-r-OEGA copolymers with HFBA/OEGA molar ratios of 5/1, 10/1, and 20/1. Compared with PHFBA and POEGA, the mechanical strength and toughness of the three copolymers are considerably enhanced. The PHFBA-r-OEGA with the HFBA/OEGA molar ratio of 10/1 possesses the maximum mechanical strength (Figure S10b, Supporting Information), which is much higher than that of PHFBA. The undesired mechanical performance of PHFBA is probably due to that the strong electron-withdrawing effect of F atoms in HFBA monomers affecting the electrons of double bonds, leading to the lower reactivity of fluorinated (meth)acrylates than that of hydrogenated homologs.[27] Considering the high mechanical strength, PHFBA-r-OEGA with the HFBA/OEGA molar ratio of 10/1 was selected as an optimal copolymer network for the ICFE.

Mechanical properties of ICFE can be further regulated by tailoring the LiTFSI concentration within the ICFE. Figure 3d shows the tensile stress–strain curves of PHFBA-r-OEGA and ICFE. The elongation at break, mechanical strength and toughness of the ICFE increase simultaneously as the LiTFSI concentration increases from 0.5 to 1.5 M. The ICFE-0.5M exhibits an elongation at break of ≈3155% with a mechanical strength of ≈367 kPa and toughness of ≈4.7 MJ m^{-3}, whereas the elongation at break of ICFE-1.5M reaches up to ≈6000%, together with the high mechanical strength of ≈770 kPa and high toughness of ≈17.1 MJ m^{-3} (Figure S11, Supporting Information). The increase of LiTFSI concentration greatly improves the mechanical performance of ICFE due to the increasing number of coordinating bonds, thus improving the energy dissipation. However, the excessed LiTFSI limits the movements of polymer segments and reduces the elongation at break to ≈4775% upon the addition of 2 M LiTFSI. Besides, the low mechanical strength of ≈495 kPa and toughness of ≈9.2 MJ m^{-3} for ICFE-2M are ascribed to the decreased crystallinity, which is proved by the XRD results. The ICFE-1.5M exhibits an ultrastretchability, excellent mechanical strength, and high toughness, and thus was selected for further characterizations.

The ICFE also exhibits impressive resilience as shown in Movie S2 (Supporting Information, speed of 20 times the real time). The successive stretching/releasing processes at

a 100% strain for 500 cycles were carried out to assess the anti-fatigue ability of ICFE-1.5M. The ICFE-1.5M shows a slightly decreased stress and a small plastic deformation (<10%) (Figure S12, Supporting Information), indicating its outstanding fatigue resistance. Figure 3e displays the cyclic tensile stress–strain curves of ICFE-1.5M under various strains (100, 300, 500, 700, 1000%, respectively), and the hysteresis areas of these curves increase significantly with the increasing strains. Subsequently, the cyclic tensile tests further quantitatively evaluate the self-recovery capability of ICFE-1.5M under a relatively small strain of 500% and a large strain of 4000%. The ICFE-1.5M achieves a hysteresis ratio of 87.4% after two continuous cycles upon being stretched at 500% strain with the resting time of 30 min (Figure S13, Supporting Information). Surprisingly, the hysteresis ratio reaches up to 80.4% after 10 successive loading/unloading cycles upon being stretched to 4000% strain with the subsequent resting time of 2 h (Figure 3f). The rapid self-recovery capability could be ascribed to the reversible reconstruction of dynamic bonds within the ICFE-1.5M. Meanwhile, the microcrystalline domains prevent an irreversible sliding of polymer chains, enabling the ICFE-1.5M with impressive resilience. Furthermore, the mechanoresponsive behaviors of ICFE-1.5M were characterized by XRD analysis under different strains (Figure 3g). When the ICFE-1.5M was stretched up to 100% strain, the diffraction peak intensity has no apparent change. It is believed that the breakage of hydrogen bonds is companied in ICFE-1.5M under a 100% elastic deformation (Figure S14, Supporting Information). With further stretching ICFE-1.5M up to 200% strain and higher, the diffraction peak intensity increases distinctly, and the crystallinity (χ_c, Equation S2, Supporting Information) increases from 25.6% to 37.5%. The results indicate that stress-induced crystallization occurs in the ICFE-1.5M under large strains, which increases the energy barrier for the damage of ICFE-1.5M.[28]

For flexible ionic conductors used in wearable ionic skins, tearing resistance is of great significance to protect them from external attacks.[29] Rivlin-Thomas pure-shear tests were performed to assess the fracture energy of ICFE-1.5M (Figure 3h, Movie S3 in Supporting Information, speed of 20 times the real time).[14d,30] The notched ICFE-1.5M can be successfully stretched to L_c of 216.7 mm (L_c indicating the critical displacements at which the notch turns into a running crack) with impressive fracture energy of ≈22.3 kJ m^{-2}. Intriguingly, the ICFE-1.5M exhibits relatively high fracture energy and toughness among the reported stretchable ionic conductors (Table S5, Supporting Information).[14a-c,31] Figure 3i shows the images of the notched ICFE-1.5M under different tensile strains (200, 400, 1000, 2000, and 2500%). It can be clearly observed that the notch is dramatically blunted and remains stable, indicating the extraordinary tearing resistance of ICFE-1.5M, which is attributed to the effective energy dissipation of dynamic bonds and the stress-induced crystallization during stretching, thus preventing the crack propagation.[29a,32]

Self-healing is an ideal property for prolonging the lifespan of materials.[33] Benefiting from dynamic hydrogen bonds and coordination, the ICFE exhibits autonomous healability at room temperature. **Figure 4**a shows that two ICFE-1.5M strips are healed in 30 min without any external stimuli, and can be stretched to twice their original length. Figure 4b records the self-healing process of ICFE-1.5M using an optical microscope. The crack at the damaged interface almost disappears after 5 h at a constant temperature of 25 °C by simulating the room temperature. Furthermore, the self-healability of ICFE-1.5M under various healing time (3, 5, 7, 12 h) was quantitatively evaluated by typical tensile tests (Figure 4c). The mechanical performance of the healed ICFE-1.5M gradually recovers with the increase of healing time. After 12 h, the toughness and elongation at break of the healed ICFE-1.5M nearly restore to the original values. Figure 4d depicts the capability of the electrical recovery of

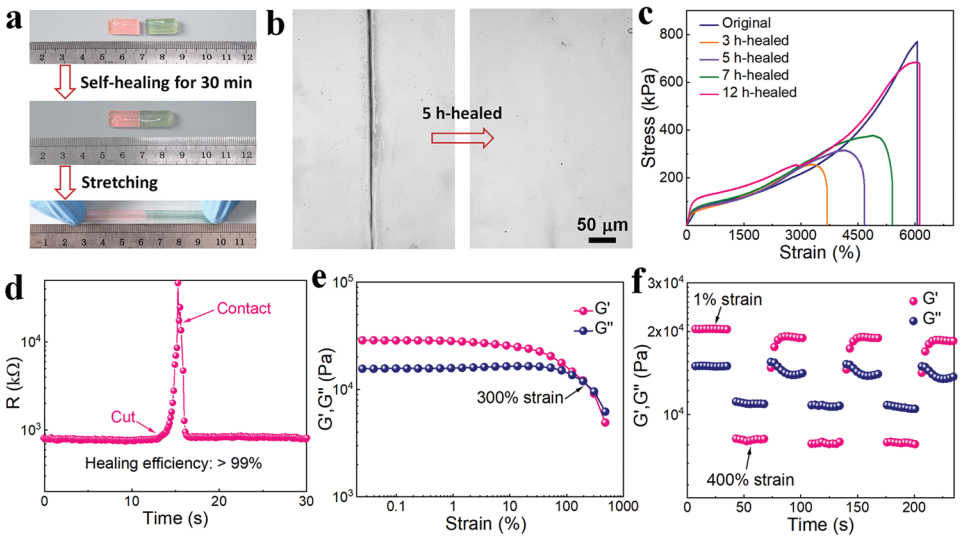

Figure 4. Room-temperature self-healing performance. a) Strip ICFE-1.5M after cutting and self-healing process. b) Optical microscope images of ICFE-1.5M upon cutting and self-healing for 5 h. c) Typical stress–strain curves of original and healed ICFE-1.5M for various healing time. d) Resistance changes of ICFE-1.5M before fracture and after self-healing. e) Rheological strain sweeping measurement of ICFE-1.5M at an angular frequency of 1 rad s^{-1}. f) Rheological step strain measurement of ICFE-1.5M with alternating shear strains of 1% and 400%.

ICFE-1.5M upon a cutting/healing cycle. The electrical healing efficiency of ICFE-1.5M reaches up to 99% within 4 s, revealing its rapid electrical recovery capability.[34]

Dynamic rheological measurements were performed to evaluate the self-healability of the ICFE. The G' and G'' of ICFE-1.5M were determined by strain sweep measurements. Figure 4e displays that the G' values are higher than the G'' values at a small shear strain (<300%), indicating the excellent structural integrity of ICFE-1.5M.[35] When the shear strain further increases to 300%, the G' values begin to decline and are smaller than the G'' values. The crossover point of G' and G'' values reveals a critical point of solid-liquid transition. Cyclic step strain measurements of ICFE-1.5M were performed, as the results presented in Figure 4f. Small (1%) and large (400%) shear strains are alternatively applied to the ICFE-1.5M, and both are maintained for 25 s. The G' and G'' values instantly return to their initial values when the shear strain is back to 1%. The following three factors might be contributed to the outstanding self-healability of ICFE: 1) the presence of abundant hydrogen bonds between the fluorinated segments;[18b] 2) the presence of coordinating bonds between Li^+ ions and ether segments;[15a] 3) the low T_g at ≈–28.2 °C of ICFE-1.5M with high mobility of polymer chains.

Hydration issues under high humidity environments are almost inevitable for hydrogels or ionogels,[29a,36] leading to the morphology, mechanical performance and ionic conductivity completely being changed. Benefiting from the continuous hydrophobic nanodomains in the ICFE, the hydration issue could be greatly alleviated. Water contacting measurements were performed to investigate the hydrophobicity of the surface of ICFEs (Figure S15, Supporting Information). The contact angles of the ICFE-0.5M, ICFE-1M, ICFE-1.5M, and ICFE-2M were calculated as 102 ± 2.9°, 100 ± 2.2°, 100 ± 3.8°, and 98 ± 2.5°, respectively, further confirming the hydrophobic nature of ICFEs. The hydrophobicity of ICFEs is originated from the surface-enriched hydrophobic fluorinated microphases during the process of film formation because fluorine-containing segments would be enriched at the interface between the polymer and air to obtain a stable surface with relatively low surface energy.[37] Underwater swelling tests were carried out to evaluate the waterproofness of ICFE-1.5M. **Figure 5**a displays the weight change of ICFE-1.5M and POEGA-1.5M stored in large amounts of water over time. The weight ratio (Equation S4, Supporting Information) of ICFE-1.5M is about 108.9% after 60 d, while that of POEGA-1.5M is more than 1500% after only 3 d, as the morphologies shown in the insets. The shape of ICFE-1.5M is almost unchanged during the testing, demonstrating its outstanding waterproofness. Humidity-controlled dynamic thermomechanical analysis (DMA-RH) was used to study the structural integrity of ICFE-1.5M under various relative humidity (Figure S16, Supporting Information). The G' values of ICFE-1.5M have no significant changes in a relative humidity range from 10% to 80%, indicating the good structural integrity of ICFE-1.5M in a wide humidity range.

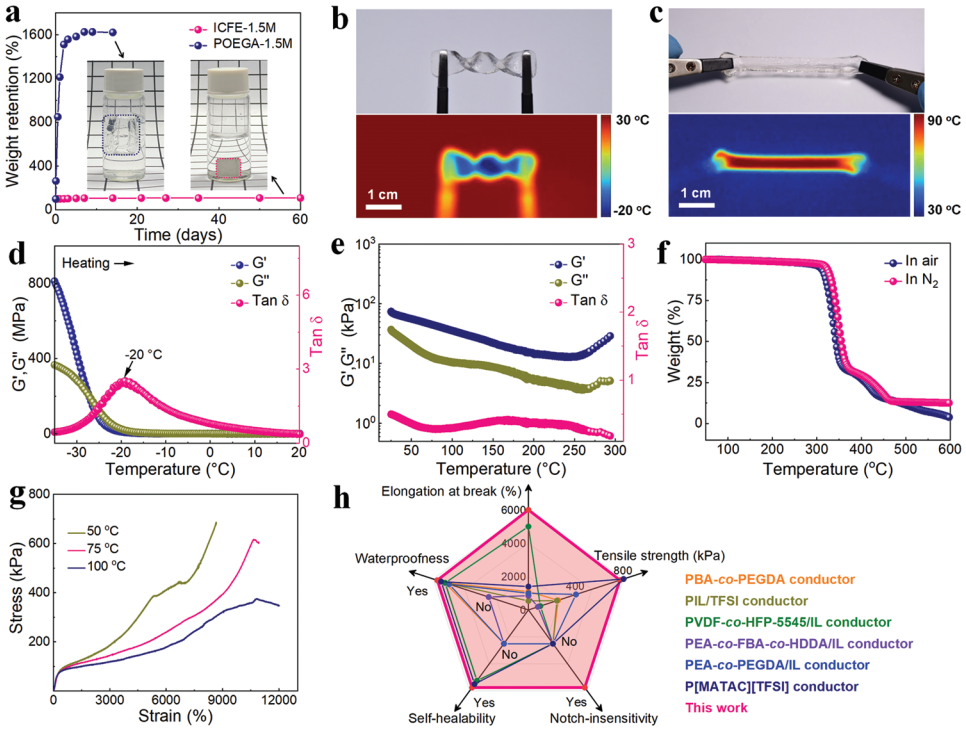

Figure 5. Extreme-temperature tolerance. a) Waterproof performance of ICFE-1.5M and POEGA-1.5M for various time. Insets showing digital photographs of ICFE-1.5M and POEGA-1.5M after being stored in water for 60 and 14 d, respectively. Digital photographs and corresponding infrared images of ICFE-1.5M at b) –20 °C and c) 90 °C, respectively. DMA curves of ICFE-1.5M d) from –35 to 20 °C and e) from 25 to 300 °C, respectively. f) TGA curves of ICFE-1.5M from 35 to 600 °C in the N_2 and air, respectively. g) Tensile stress–strain curves of ICFE-1.5M from 50 to 100 °C. h) Comparisons between the ICFE and previously reported stretchable ionic conductors in terms of elongation at break, tensile strength, notch-insensitivity, self-healability, and waterproofness.

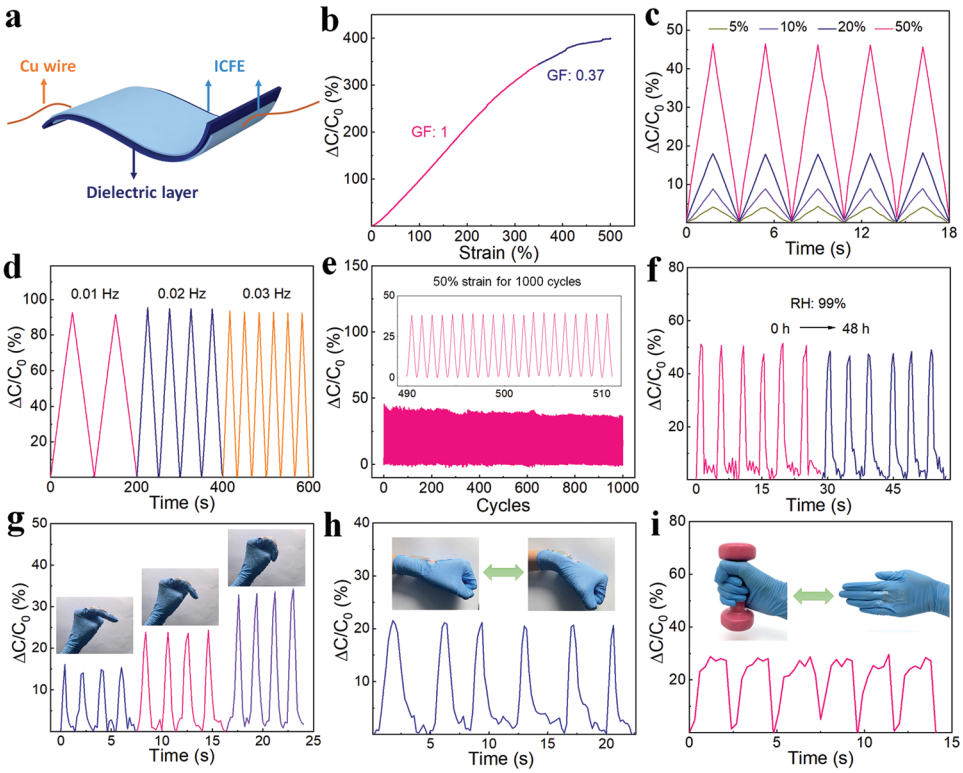

Figure 6. Wearable capacitive-type strain sensing performance. a) Schematic diagram of the structure of as-assembled capacitive-type strain sensor. b) Relative capacitance variations as a function of applied strains. c) Capacitance responses with various applied strains. d) Capacitance responses at a constant strain of 100% with various applied frequencies. e) Durability tests of the sensor under 50% strain for 1000 cycles. Inset showing the capacitance change from 490th to 510th cycles. f) Real-time capacitance responses for monitoring of finger bending before and after storing at RH of 99% for 48 h. Real-time capacitance signals of the sensor monitoring of g) finger, h) wrist, and i) palm bending, respectively. Insets showing digital photographs of the sensor clinging to the finger, wrist, and palm of a volunteer, respectively.

In addition to waterproof performance, it is also important for ionic conductors to possess high flexibility at low and high temperatures. The ICFE-1.5M endures twist deformation as low as −20 °C (Figure 5b) and stretching deformation up to 90 °C (Figure 5c). To determine the mechanical flexibility of ICFE-1.5M more accurately under the low and high temperatures, dynamic thermomechanical analysis (DMA) measurements were conducted from −35 to 20 °C and from 25 to 300 °C, respectively. Figure 5d shows that the G' and G'' values of ICFE-1.5M decrease sharply with the increasing temperatures from −35 to 20 °C, and the Tan δ reaches the peak at −20 °C, where the ICFE-1.5M changes from the glassy state to elastic state (i.e., transition temperature). That is, the mechanical flexibility of ICFE-1.5M is well maintained above −20 °C, revealing its excellent freeze-resistant performance. Figure 5e shows that the G' of ICFE-1.5M is always higher than that of G'' even the temperature is up to 300 °C, indicating high-temperature tolerance of ICFE-1.5M. This is because the fluorinated PHFBA-r-OEGA backbone has a heat-resistant performance.[38] In addition, a slight increase in the G' and G'' values of ICFE-1.5M with the temperature increasing from 260 to 300 °C is probably due to the increase of crosslinking density caused by oxidative cross-linking of polymer chains under such high temperatures. Based on the DMA results, it can be concluded that the ICFE exhibits high mechanical flexibility and outstanding heat/freeze-resistant performance in a wide temperature range of −20 to 300 °C.

The thermal stability of ICFE-1.5M in nitrogen and air was assessed using thermogravimetric analysis (TGA) with temperatures ranging from 35 to 600 °C. The ICFE-1.5M shows an ultrahigh decomposition temperature of ≈315 °C in N_2 and ≈300 °C in the air (Figure 5f). Figure 5g shows the tensile stress–strain curves of the ICFE-1.5M at high temperatures (50, 75, 100 °C, respectively). When the temperature increases from 50 to 100 °C, the elastic modulus of the ICFE-1.5M exhibits a decrease due to the enhanced mobility of polymer chains under high temperatures. However, the ICFE-1.5M at the temperature of 100 °C still shows a notably high elongation of ≈12 000% with a mechanical strength of ≈347 kPa. Moreover, the ICFE-1.5M is thermally stable and its weight maintains at 25, 50, and 100 °C in the open air for long-term testing of 30 d (Figure S17, Supporting Information). To demonstrate the advantages of ICFE among the reported stretchable ionic conductors, the ICFE is compared in detail concerning elongation at break, tensile strength, notch-insensitivity, self-healability, and waterproofness (Figure 5h).[8,14a,b,18b,39] To our best knowledge, the liquid-free ICFE based on the hydrophobicity-constrained association strategy has never been proposed, which will spur much research attention in the exploration of high-performance ionic conductors for wearable ionic skins.

Benefiting from extraordinary mechanical versatility and outstanding tolerance to extreme environments, the ICFE is capable of being assembled into a capacitive-type strain sensor. The ICFE-based sensor was assembled with a dielectric layer (VHB 4910, 3M) sandwiched with two ICFE films, and two copper current collectors were used for connecting test wires (**Figure 6**a). The outstanding stretchability of ICFE-1.5M enables the ICFE sensor with a broad detection range (0–500%) (Figure 6b), which is much higher than those of other capacitance sensors.[22,36a] Two different stages of the sensing performance are observed. In the strain range of 0–350%, the relative capacitance variation ($\Delta C/C_0$) linearly increases with the strains, and the gauge factor (GF) is calculated as ≈1, which is consistent with the theoretical prediction.[6a,40] In the strain range of 350–500%, the GF gradually drops to 0.37, which is mainly attributed to the low permittivity of dielectric layers at the large strain.[40]

Figure 6c depicts the evolution of $\Delta C/C_0$ signals of the ICFE capacitance sensor during the successive stretching/releasing cycles with the increasing strain from 5% to 50%, and repeatable and rapid $\Delta C/C_0$ signals are observed. The ICFE capacitance sensor is measured at various frequencies to simulate the actual sensing processes in dynamic continuous strain detection. A highly stable and reliable response upon 100% strain with a stretching frequency ranging from 0.01 to 0.03 Hz is acquired, revealing the frequency-independent sensing performance of the ICFE sensor (Figure 6d). The ICFE capacitance sensor also shows fast response time (≈0.3 s) and recovery time (≈0.6 s) upon a 10% strain owing to its excellent resilience (Figure S18, Supporting Information). Figure S19 (Supporting Information) depicts the capacitance signals (C/C_0) of the sensor in the temperature range of 10–80 °C. The signals remain almost unchanged under a variety of temperatures, illustrating that the ICFE-based sensor is insensitive to the temperature variation since the capacitance values of parallel-plate capacitors are independent of environmental temperatures. To confirm the durability and mechanical stability, 50% strain for 1000 cycles was applied to the ICFE capacitance sensor (Figure 6e). The inset clearly shows that the $\Delta C/C_0$ signals from 490th to 510th cycles keep similar waveforms and amplitudes, indicating excellent reliability of the ICFE capacitance sensor during long-term stretching/releasing cycles.

For human-machine interfaces, wearable sensors are expected to connect with human skin or various substrates and realize human-motion detection.[30,41] Intriguingly, the ICFE has outstanding adhesive capacities, which is capable of being adhered tightly to both hydrophobic and hydrophilic substrate surfaces of silicone rubber, stainless steel, polytetrafluoroethylene (PTFE), ceramic, rubber, and wood (Figure S20a, Supporting Information). Besides, the ICFE exhibits an impressive adhesive ability on the skin of a volunteer without any residue when being peeled off (Figure S20b, Supporting Information). Thus, the ICFE sensor is a promising wearable ionic sensor for monitoring various human movements due to the superior adhesiveness and waterproofness of ICFE as well as the outstanding sensing performance of the sensor.

Figure 6f shows that the ICFE sensor is utilized to detect the finger straightening/bending processes before and after being stored at 99% relative humidity for 48 h. Similar waveforms and amplitudes generated by the ICFE sensor are observed, indicating its humidity-independent sensing performance. To further confirm the waterproof performance of the ICFE sensor, the sensor was immersed in water for various periods (0, 6, and 12 h) and then to monitor the elbow bending of a volunteer (Figure S21, Supporting Information). The $\Delta C/C_0$ signals are kept steadily for four straightening/bending cycles after the various immersion time, indicating its high reliability and waterproofness even after long-term immersion in water. This is ascribed to the presence of the hydrophobic fluorinated microphase among the ICFE. Figure 6g depicts the detection of the finger bending with different bending angles. The $\Delta C/C_0$ signal waves increase with the increased bending angles of the finger and remain stable when the finger is maintained at a certain angle. Figure 6h shows that the ICFE sensor has no hysteresis of $\Delta C/C_0$ signals during the successive wrist straightening/bending processes. Moreover, the ICFE sensor is attached to a palm, and the process of picking up a dumbbell produces fully steady capacitance variations (Figure 6i). Overall, the ICFE exhibits great potential to promote the capacitance sensor towards the practical application of wearable sensors.

3. Conclusion

In summary, we present a hydrophobicity-constrained association strategy for fabricating the ICFE with hierarchically responsive microphase-separated nanodomains, which consist of the hydrophobic fluorinated nanodomains and the hydrophilic polyether nanodomains. Due to the coordination and "fluorous effect," the Li^+ and $TFSI^-$ ions are selectively enriched in the hydrophilic nanodomain and hydrophobic nanodomain, respectively. The hydrophilic nanodomain with long-range ordering is employed as a high-efficient transport channel of Li^+ ions, yielding a superior ionic conductivity of 3.5×10^{-3} S m^{-1} at 25 °C for the ICFE. Moreover, the ionic conductivity is enhanced by an increase in the lithium salt concentrations and the OEGA contents among the ICFE. The 3D continuous hydrophobic nanodomains imbue the ICFE with unique waterproofness and high-temperature tolerance up to 300 °C. In addition, the ICFE also exhibits freeze-resistant performance to −20 °C because it is liquid-free. Furthermore, the preferential ruptures of the hydrogen bonds and the stress-induced crystallization endow the ICFE with supreme damage-tolerant capacity. As a result, the ICFE exhibits ultrastretchability (>6000%), high strength (770 kPa), high toughness (17.1 MJ m^{-3}), superior fracture energy (22.3 kJ m^{-2}), antifatigue ability (10% plastic deformation during consecutive stretching/releasing processes at a 100% strain for 500 cycles), excellent elasticity, rapid recoverability (80.4% hysteresis ratio after 10 successive tensile cycles upon a 4000% tensile strain for 2 h resting time), and room-temperature self-healability (100% healing efficiency after cutting and self-healing for 12 h). Owing to its outstanding mechanical elasticity and high tolerance to harsh environments, the ICFE can readily work as a waterproof stretchable ionic conductor for the skin-inspired capacitive-type ionic sensor. The sensor achieves high sensitivity and linear response (GF value up to 1 over a wide strain range of 0–350%), fast response time (0.3 s), excellent durability (>1000 cycles), and unique waterproofness with stable capacitance responses after immersion in water for

various periods (0, 6, and 12 h). Besides, the sensor is capable of monitoring complex human motions of finger, wrist and palm bendings rapidly and in real-time. The developed hydrophobicity-constrained association strategy opens a new avenue to fabricate liquid-free ion-conducting elastomers for highly stretchable and harsh-environment tolerant ionic skins.

4. Experimental Section

Preparation of the ICFE: LiTFSI was dissolved in the mixed solution of HFBA and OEGA, forming a transparent precursor solution. The precursor solution was injected into a Teflon mold upon the addition of DEAP and cured by ultraviolet light irradiation (365 nm, 8 W) for 2 h. The ICFE-0.5M, ICFE-1M, ICFE-1.5M, and ICFE-2M represent the resultant ICFE samples prepared with the addition of 0.5, 1, 1.5, and 2 M LiTFSI, respectively. The HFBA/OEGA molar ratio was tailored at 5/1, 10/1, and 20/1, respectively. The molar percentage of the DEAP to the total monomers was set at 2%. For comparison, the POEGA and POEGA-1.5M (POEGA containing 1.5 M LiTFSI) were prepared by using the same procedure as the ICFE. The PHFBA and PHFBA-1.5M (PHFBA containing 1.5 M LiTFSI) were also prepared by using relatively high initiator dosages and prolonged polymerization time because of the low polymerization reactivity of HFBA. Specifically, the molar percentage of the DEAP to HFBA and the polymerization time of HFBA were set at 3% and 6 h, respectively. This study was approved by the Institutional Review Board of Wuxi School of Medicine of Jiangnan University (LS20211028). All participants have signed a written informed consent for conducting human skin-attachment experiments.

Supporting Information

Supporting Information is available from the Wiley Online Library or from the author.

Acknowledgements

The authors acknowledge funding support from the National Natural Science Foundation of China (52122303 and 21875033).

Conflict of Interest

The authors declare no conflict of interest.

Data Availability Statement

The data that support the findings of this study are available from the corresponding author upon reasonable request.

Keywords

fluorinated elastomers, harsh environment tolerance, self-healable, skin-inspired ionotronics, stretchable ionic conductors

Received: December 2, 2021
Revised: January 24, 2022
Published online:

[1] S. Wang, J. Xu, W. Wang, G.-J. N. Wang, R. Rastak, F. Molina-Lopez, J. W. Chung, S. Niu, V. R. Feig, J. Lopez, T. Lei, S.-K. Kwon, Y. Kim, A. M. Foudeh, A. Ehrlich, A. Gasperini, Y. Yun, B. Murmann, J. B. H. Tok, Z. Bao, *Nature* **2018**, *555*, 83.

[2] a) Z. Xie, R. Avila, Y. Huang, J. A. Rogers, *Adv. Mater.* **2020**, *32*, 1902767; b) H. Zhang, Y. Cong, A. R. Osi, Y. Zhou, F. Huang, R. P. Zaccaria, J. Chen, R. Wang, J. Fu, *Adv. Funct. Mater.* **2020**, *30*, 1910573; c) C. Xie, X. Wang, H. He, Y. Ding, X. Lu, *Adv. Funct. Mater.* **2020**, *30*, 1909954.

[3] S. Wang, Y. Gao, A. Wei, P. Xiao, Y. Liang, W. Lu, C. Chen, C. Zhang, G. Yang, H. Yao, T. Chen, *Nat. Commun.* **2020**, *11*, 4359.

[4] a) Y. Gao, F. Guo, P. Cao, J. Liu, D. Li, J. Wu, N. Wang, Y. Su, Y. Zhao, *ACS Nano* **2020**, *14*, 3442; b) Y. Ren, J. Guo, Z. Liu, Z. Sun, Y. Wu, L. Liu, F. Yan, *Sci. Adv.* **2019**, *5*, eaax0648.

[5] a) N. Matsuhisa, X. Chen, Z. Bao, T. Someya, *Chem. Soc. Rev.* **2019**, *48*, 2946; b) C. Wang, C. Wang, Z. Huang, S. Xu, *Adv. Mater.* **2018**, *30*, 1801368; c) Y. Wang, Y. Yu, J. Guo, Z. Zhang, X. Zhang, Y. Zhao, *Adv. Funct. Mater.* **2020**, *30*, 2000151.

[6] a) Z. Lei, P. Wu, *Nat. Commun.* **2019**, *10*, 3429; b) C. Keplinger, J.-Y. Sun, C. C. Foo, P. Rothemund, G. M. Whitesides, Z. Suo, *Science* **2013**, *341*, 984; c) H. J. Kim, B. Chen, Z. Suo, R. C. Hayward, *Science* **2020**, 367, 773.

[7] a) Z. Cao, H. Liu, L. Jiang, *Mater. Horiz.* **2020**, *7*, 912; b) Y. Ren, Z. Liu, G. Jin, M. Yang, Y. Shao, W. Li, Y. Wu, L. Liu, F. Yan, *Adv. Mater.* **2021**, *33*, 2008486.

[8] X. Ming, L. Shi, H. Zhu, Q. Zhang, *Adv. Funct. Mater.* **2020**, *30*, 2005079.

[9] a) K. He, S. H.-S. Cheng, J. Hu, Y. Zhang, H. Yang, Y. Liu, W. Liao, D. Chen, C. Liao, X. Cheng, Z. Lu, J. He, J. Tang, R. K. Y. Li, C. Liu, *Angew. Chem., Int. Ed.* **2021**, *60*, 12116; b) J. Wan, J. Xie, X. Kong, Z. Liu, K. Liu, F. Shi, A. Pei, H. Chen, W. Chen, J. Chen, X. Zhang, L. Zong, J. Wang, L.-Q. Chen, J. Qin, Y. Cui, *Nat. Nanotechnol.* **2019**, *14*, 705; c) C. Zhang, H. Zheng, J. Sun, Y. Zhou, W. Xu, Y. Dai, J. Mo, Z. Wang, *Adv. Mater.* **2022**, *34*, 2105996; d) P. Zhang, W. Guo, Z. H. Guo, Y. Ma, L. Gao, Z. Cong, X. J. Zhao, L. Qiao, X. Pu, Z. L. Wang, *Adv. Mater.* **2021**, *33*, 2101396.

[10] a) J. Zhu, G. Y. Chen, L. Yu, H. Xu, X. Liu, J. Sun, *CCS Chem.* **2020**, *2*, 280; b) Z. Li, Y. L. Zhu, W. Niu, X. Yang, Z. Jiang, Z. Y. Lu, X. Liu, J. Sun, *Adv. Mater.* **2021**, *33*, 2101498.

[11] S. Gao, F. Sun, N. Liu, H. Yang, P.-F. Cao, *Mater. Today* **2020**, *40*, 140.

[12] Z. Stoeva, I. Martin-Litas, E. Staunton, Y. G. Andreev, P. G. Bruce, *J. Am. Chem. Soc.* **2003**, *125*, 4619.

[13] C. V. Amanchukwu, Z. Yu, X. Kong, J. Qin, Y. Cui, Z. Bao, *J. Am. Chem. Soc.* **2020**, *142*, 7393.

[14] a) X. Qu, W. Niu, R. Wang, Z. Li, Y. Guo, X. Liu, J. Sun, *Mater. Horiz.* **2020**, *7*, 2994; b) L. Shi, T. Zhu, G. Gao, X. Zhang, W. Wei, W. Liu, S. Ding, *Nat. Commun.* **2018**, *9*, 2630; c) B. Yiming, Y. Han, Z. Han, X. Zhang, Y. Li, W. Lian, M. Zhang, J. Yin, T. Sun, Z. Wu, T. Li, J. Fu, Z. Jia, S. Qu, *Adv. Mater.* **2021**, *33*, 2006111; d) P. Zhang, Y. Chen, Z. H. Guo, W. Guo, X. Pu, Z. L. Wang, *Adv. Funct. Mater.* **2020**, *30*, 1909252.

[15] a) Y. Shi, Y. Wang, Y. Gu, L. Zheng, S. Ma, X. Xu, *Chem. Eng. J.* **2020**, *392*, 123645; b) X. Cao, J. Yang, R. Wang, X. Zhang, J. Xu, *Polymer* **2019**, *180*, 121745.

[16] P. Shi, Y. Wang, W. W. Tjiu, C. Zhang, T. Liu, *ACS Appl. Mater. Interfaces* **2021**, *13*, 49358.

[17] a) I. Osada, H. de Vries, B. Scrosati, S. Passerini, *Angew. Chem., Int. Ed.* **2016**, *55*, 500; b) X. Fan, X. Ji, L. Chen, J. Chen, T. Deng, F. Han, J. Yue, N. Piao, R. Wang, X. Zhou, X. Xiao, L. Chen, C. Wang, *Nat. Energy* **2019**, *4*, 882; c) C. H. Li, J. L. Zuo, *Adv. Mater.* **2020**, *32*, 1903762.

[18] a) M. Karaman, M. GÜRsoy, F. AykÜL, Z. Tosun, M. D. Kars, H. B. Yildiz, *Plasma Sci. Technol.* **2017**, *19*, 085503; b) Y. Cao,

T. G. Morrissey, E. Acome, S. I. Allec, B. M. Wong, C. Keplinger, C. Wang, *Adv. Mater.* **2017**, *29*, 1605099.
[19] C. Z. Zhao, X. Q. Zhang, X. B. Cheng, R. Zhang, R. Xu, P. Y. Chen, H. J. Peng, J. Q. Huang, Q. Zhang, *Proc. Natl. Acad. Sci USA* **2017**, *114*, 11069.
[20] Y. Wang, Y. Liu, R. Plamthottam, M. Tebyetekerwa, J. Xu, J. Zhu, C. Zhang, T. Liu, *Macromolecules* **2021**, *54*, 3832.
[21] a) Y. Wang, M. Tebyetekerwa, Y. Liu, M. Wang, J. Zhu, J. Xu, C. Zhang, T. Liu, *Chem. Eng. J.* **2020**, *420*, 127637; b) D. Liu, X. Dong, B. Han, H. Huang, M. Qi, *Compos. Commun.* **2020**, *21*, 100374.
[22] Z. Lei, P. Wu, *Nat. Commun.* **2018**, *9*, 1134.
[23] D. G. Mackanic, X. Yan, Q. Zhang, N. Matsuhisa, Z. Yu, Y. Jiang, T. Manika, J. Lopez, H. Yan, K. Liu, X. Chen, Y. Cui, Z. Bao, *Nat. Commun.* **2019**, *10*, 5384.
[24] D. H. C. Wong, J. L. Thelen, Y. Fu, D. Devaux, A. A. Pandya, V. S. Battaglia, N. P. Balsara, J. M. DeSimone, *Proc. Natl. Acad. Sci USA* **2014**, *111*, 3327.
[25] R. C. Agrawal, G. P. Pandey, *J. Phys. D* **2008**, *41*, 223001.
[26] K. Li, Z. Zhu, R. Zhao, H. Du, X. Qi, X. Xu, L. Qie, *Energy Environ. Mater.* **2021**, *5*, 337.
[27] a) B. Guyot, B. Améduri, B. Boutevin, A. Sidéris, *Macromol. Chem. Phys.* **1995**, *196*, 1875; b) B. Guyot, B. Ameduri, B. Boutevin, M. Melas, M. Viguier, A. Collet, *Macromol. Chem. Phys.* **1998**, *199*, 1879.
[28] a) X. Zhou, B. Guo, L. Zhang, G.-H. Hu, *Chem. Soc. Rev.* **2017**, *46*, 6301; b) E. Ducrot, Y. Chen, M. Bulters, R. P. Sijbesma, C. Creton, *Science* **2014**, *344*, 186.
[29] a) S. Chen, L. Sun, X. Zhou, Y. Guo, J. Song, S. Qian, Z. Liu, Q. Guan, E. M. Jeffries, W. Liu, Y. Wang, C. He, Z. You, *Nat. Commun.* **2020**, *11*, 1107; b) Z. Xu, M. Wu, W. Gao, H. Bai, *Adv. Mater.* **2020**, *32*, 2002695.
[30] Y. Xu, Q. Feng, C. Zhang, T. Liu, *Compos. Commun.* **2021**, *25*, 100693.
[31] a) Y. Guo, X. Qu, Z. Hu, J. Zhu, W. Niu, X. Liu, *J. Mater. Chem. A* **2021**, *9*, 13597; b) J. Huang, S. Peng, J. Gu, G. Chen, J. Gao, J. Zhang, L. Hou, X. Yang, X. Jiang, L. Guan, *Mater. Horiz.* **2020**, *7*, 2085; c) B. Yiming, X. Guo, N. Ali, N. Zhang, X. Zhang, Z. Han, Y. Lu, Z. Wu, X. Fan, Z. Jia, S. Qu, *Adv. Funct. Mater.* **2021**, *31*, 2102773.
[32] a) C. Creton, *Macromolecules* **2017**, *50*, 8297; b) X. Li, K. Cui, T. L. Sun, L. Meng, C. Yu, L. Li, C. Creton, T. Kurokawa, J. P. Gong, *Proc. Natl. Acad. Sci. USA* **2020**, *117*, 7606.
[33] a) Z. Liu, L. Zhang, Q. Guan, Y. Guo, J. Lou, D. Lei, S. Wang, S. Chen, L. Sun, H. Xuan, E. M. Jeffries, C. He, F. L. Qing, Z. You, *Adv. Funct. Mater.* **2019**, *29*, 1901058; b) W. Niu, Y. Zhu, R. Wang, Z. Lu, X. Liu, J. Sun, *ACS Appl. Mater. Interfaces* **2020**, *12*, 30805.
[34] X. Dai, L.-B. Huang, Y. Du, J. Han, J. Kong, *Compos. Commun.* **2021**, *24*, 100654.
[35] B. Zhang, X. Zhang, K. Wan, J. Zhu, J. Xu, C. Zhang, T. Liu, *Research* **2021**, *2021*, 9761625.
[36] a) J. Mao, C. Zhao, Y. Li, D. Xiang, Z. Wang, *Compos. Commun.* **2020**, *17*, 22; b) A. Wang, Y. Wang, B. Zhang, K. Wan, J. Zhu, J. Xu, C. Zhang, T. Liu, *Chem. Eng. J.* **2021**, *411*, 128506; c) L. Li, J. Meng, M. Zhang, T. Liu, C. Zhang, *Chem. Commun.* **2021**, *58*, 185.
[37] M. Karaman, T. Uçar, *Appl. Surf. Sci.* **2016**, *362*, 210.
[38] J. Qu, X. Li, Y. Cui, Q. Wang, *Int. J. Heat Mass Transfer* **2017**, *107*, 640.
[39] a) Z. Yu, P. Wu, *Adv. Mater.* **2021**, *33*, 2008479; b) L. Shi, K. Jia, Y. Gao, H. Yang, Y. Ma, S. Lu, G. Gao, H. Bu, T. Lu, S. Ding, *Research* **2020**, *2020*, 2505619.
[40] J.-Y. Sun, C. Keplinger, G. M. Whitesides, Z. Suo, *Adv. Mater.* **2014**, *26*, 7608.
[41] Q. Xia, S. Wang, W. Zhai, C. Shao, L. Xu, D. Yan, N. Yang, K. Dai, C. Liu, C. Shen, *Compos. Commun.* **2021**, *26*, 100809.